




Article

Photonic Integrated Circuit for Optical Phase Control of 1×4 Terahertz Phased Arrays

Peng Lu ¹, Thomas Haddad ¹, Jonas Tebart ¹, Chris Roeloffzen ² and Andreas Stöhr ^{1,*}¹ Department of Optoelectronics, University of Duisburg-Essen, Lotharstraße 55, 47057 Duisburg, Germany² LioniX International BV, Hengelosestraat 500, 7521 AN Enschede, The Netherlands

* Correspondence: andreas.stoehr@uni-due.de

Abstract: In this manuscript, we report on a 1×4 optical beam forming network (OBFN) chip using optical phase shifters (OPSs) based on thermo-optically controlled optical ring resonators (ORRs) for 1D beam steering at 0.3 THz. The 1×4 OBFN chip consists of four OPSs and is fabricated using TriPleX technology. Each of the four OPSs is realized by two cascaded identical ORRs, to reach a phase shift of 2π . To allow transfer of the optical phase shift to the THz domain by optical heterodyning in high-frequency $1.55 \mu\text{m}$ modified uni-travelling carrier photodiodes, the ORRs are designed such that one carrier of the optical heterodyne signal is at the ORR's resonance frequency, whereas the second optical heterodyne signal is at its off-resonance. By adjusting the resonance frequencies of the two ORRs in each OPS synchronously, a relative phase variation between two optical heterodyne carriers of up to 2π with a tuning efficiency of $0.058 \text{ W}/\pi$, is experimentally demonstrated. Due to the dispersive power transmission loss of the ORRs, phase tuning leads to a power variation of the optical heterodyne-generated signals up to 3.8 dB, which is experimentally characterized at 0.295 THz. It is shown numerically that this power variation only has a minor impact on the steering performance of a 1×4 phased array. The determined beam direction deviation and maximum absolute radiation power change are smaller than 1° and 2 dB, respectively. By sweeping the phase difference between two adjacent THz antennas in the 1×4 phased array, from -120° to 120° , a beam steering range of $\sim 62^\circ$ is demonstrated numerically at 0.295 THz.



Citation: Lu, P.; Haddad, T.; Tebart, J.; Roeloffzen, C.; Stöhr, A. Photonic Integrated Circuit for Optical Phase Control of 1×4 Terahertz Phased Arrays. *Photonics* **2022**, *9*, 902. <https://doi.org/10.3390/photonics9120902>

Received: 12 October 2022

Accepted: 23 November 2022

Published: 25 November 2022

Publisher's Note: MDPI stays neutral with regard to jurisdictional claims in published maps and institutional affiliations.



Copyright: © 2022 by the authors. Licensee MDPI, Basel, Switzerland. This article is an open access article distributed under the terms and conditions of the Creative Commons Attribution (CC BY) license (<https://creativecommons.org/licenses/by/4.0/>).

Keywords: THz beam steering; optical phase shifter; optical ring resonator; TriPleX; dielectric rod waveguide; phased array

1. Introduction

Photonic-based THz systems have been intensively investigated for various applications, e.g., communications [1,2], spectroscopy [3,4] and imaging [5], because they offer wide operational bandwidths, superior phase noise, and low loss transmission over long distances using optical fibers. For applications such as long-range THz communications, the high free-space path loss together with the limited transmit power, necessitate the use of high-gain directional THz antennas. This, in turn, requires photonic THz beam steering technologies which can be generally classified into two categories: namely frequency-steering using leaky-wave antennas (LWAs), and frequency independent steering using phased-array antennas. LWAs offer a quite attractive approach for THz beam steering, since the beam direction can be easily adjusted by tuning the operating frequency. Especially in combination with envelope detection, first high data rate mobile THz communications have been demonstrated [6]. However, for THz spectroscopy or imaging applications, frequency independent photonic THz beam steering approaches are required. In [7], fiber-based optical delay lines are used to adjust the time delays for a 1×4 photomixer array. This way, a maximum beam steering angle of 35° at 0.6 THz has been achieved. However, the fiber-based optical delay lines prevent compact integration. First, chip integrated delay

lines using Mach–Zehnder-based switched delay lines for sub-THz range, were demonstrated, e.g., in [8]. The disadvantage is that only discrete beam angles are supported, and for a high beam angle resolution, several 10 s of thermo-optical switches would be required, leading to a high-power consumption. Since the beam squint effect becomes less dominant in the THz domain [9], optical phase shifters (OPSs) for phased-array antennas have also been investigated. Using OPSs based on thermo-optically controlled straight silica waveguides [10], continuous beam steering at 0.3 THz is demonstrated, with a maximum steering angle of 50° . In this approach, only one heater is required for each OPS. However, the phase tuning efficiency of $0.24 \text{ W}/\pi$ is relatively low.

Due to the low optical propagation losses, $\text{Si}_3\text{N}_4/\text{SiO}_2$ -based TriPleX waveguides have been exploited for a number of applications, such as reconfigurable photonic RF filters [11], high-granularity wavelength division multiplexers [12], high-order ring resonators [13] and programmable optical signal processor chips [14]. Additionally, on-chip optical true time delays (TTDs) consisting of optical ring resonators (ORRs) are reported for continuous beam steering at microwave frequencies [15–17]. Using the separate carrier tuning technique, the phase shift of the optical carrier can be adjusted to compensate for the nonlinearity of the phase response of TTDs [18]. However, this approach is not easily scalable to THz frequencies, as the beam angle becomes much more sensitive to time delay variations at THz frequencies. As an example, a time delay variation of only 30 fs would lead to a beam deviation of $\sim 1^\circ$ at 0.3 THz. Consequently, to reach a constant time delay over a reasonable bandwidth, one would need to cascade a multifold of ORRs leading to higher power consumption, and substantially more complex control circuitry.

In this manuscript, we report on the design and experimental characterization of a TriPleX-based 1×4 OBFN chip with 4 OPSs for continuous beam steering at 0.3 THz. Each OPS consists of two cascaded ORRs. The fabricated OBFN chip enables the transfer of the optical phase shift to the THz domain, by optical heterodyne THz signal generation in high-frequency modified uni-traveling carrier photodiodes (MUTC-PDs). To support optical heterodyning, the ORRs are designed such that one laser signal is at the ORR's resonance frequency, while the other optical carrier of the heterodyne signal is at the off-resonance frequency. The manuscript demonstrates experimentally that the fabricated 1×4 OBFN chip yields optical phase shifts up to 2π , with a tuning efficiency of $0.058 \text{ W}/\pi$. Furthermore, the inherent THz power variation during phase tuning due to the dispersive power transmission loss of the ORRs, is experimentally characterized at 0.295 THz. It is shown numerically using CST Studio Suite that these power variations only have a negligible impact on the steering angle. It is furthermore determined numerically that the maximum beam steering angle for a 1×4 phased array employing THz bow-tie antennas, is 62° at 0.295 THz.

2. Optical Beam Forming Network Chip

The concept of the 1×4 OBFN chip with integrated MUTC-PDs for 1D beam steering at 0.3 THz, based on optical heterodyning, is shown in Figure 1a. The OBFN chip is designed and fabricated based on the $\text{Si}_3\text{N}_4/\text{SiO}_2$ TriPleX platform [19], providing a low optical propagation loss, as well as a high optical confinement factor. Optical heterodyne laser signals ($\sim 1.55 \mu\text{m}$) with a difference frequency of 0.3 THz, are combined and coupled into the OBFN chip. Three Mach–Zehnder interferometers (MZIs) are used as tunable optical splitters to adjust the power distribution into each waveguide, and to compensate for the non-uniform responsivity of the MUTC-PDs. Each OPS consists of two cascaded identical ORRs. The coupler heaters of the rings are used to change the power coupling coefficients, and thus to modify the slope of ORR's phase response. By changing the biases of the ring heaters, the ORR's resonance frequency offsets are shifted which allows it to modify the phase difference between the two optical heterodyne signals. Finally, MUTC-PDs are exploited to transfer the optical phase shift into the THz domain and by integrating the MUTC-PD array with antennas having a half-wavelength pitch, the THz beam direction can be controlled by the OBFN chip.

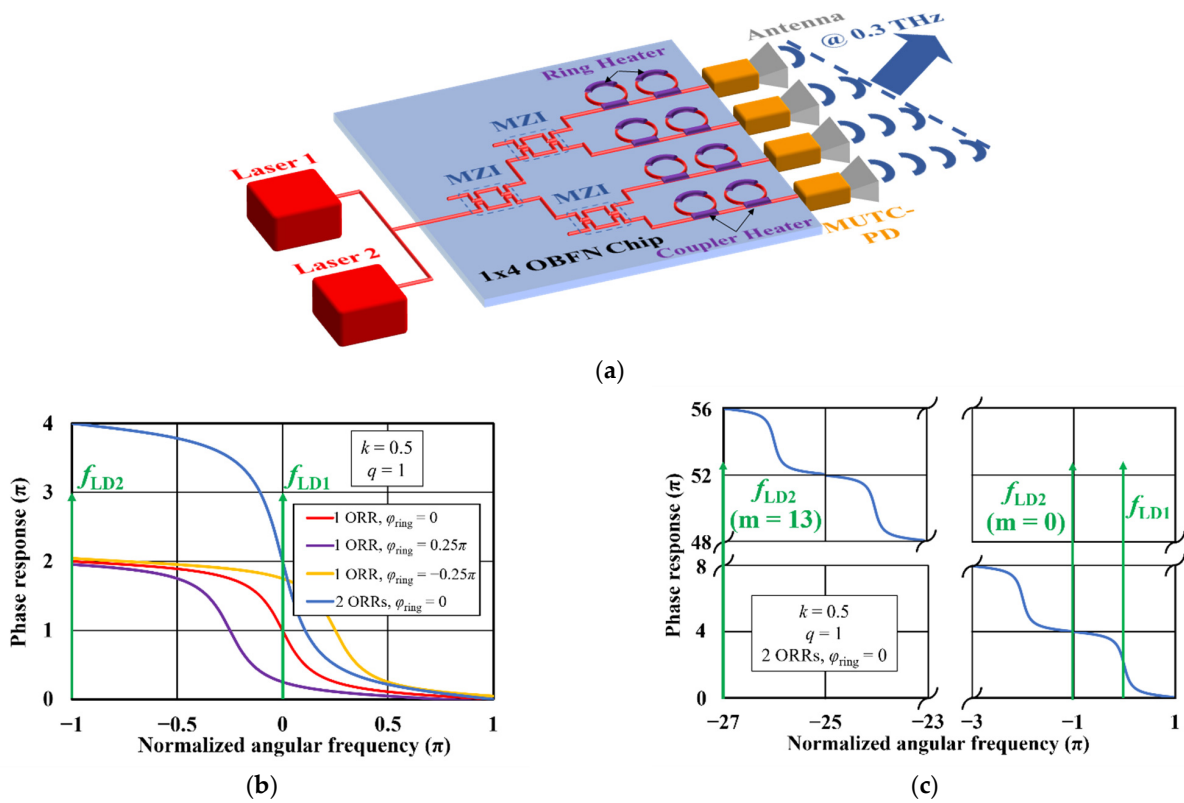


Figure 1. (a) Concept of the 1×4 OBFN chip with integrated MUTC-PDs for 1D beam steering at 0.3 THz. (b) Calculated phase response within one FSR for a single ORR with different round-trip phase shifts φ_{ring} as well as for two cascaded ORRs with the same resonance frequency. The power coupling coefficient k is 0.5 and the amplitude loss factor q is 1. (c) Calculated phase response within fourteen FSRs for two cascaded ORRs with the same resonance frequency. The power coupling coefficient k is 0.5 and the amplitude loss factor q is 1.

In detail, the phase response of a single ORR under the condition of over-coupling range can be calculated as follows [20]:

$$\varphi(\Omega) = \pi - (2\Omega + \varphi_{ring}) - \arctan \left[\frac{\sqrt{1-k} \cdot \sin(\Omega + \varphi_{ring})}{q - \sqrt{1-k} \cdot \cos(\Omega + \varphi_{ring})} \right] - \arctan \left[\frac{q \cdot \sqrt{1-k} \cdot \sin(\Omega + \varphi_{ring})}{1 - q \cdot \sqrt{1-k} \cdot \cos(\Omega + \varphi_{ring})} \right], \quad (1)$$

where Ω is the normalized angular frequency to the free spectral range (FSR) of the ORR ($\Omega = 2 \cdot \pi \cdot f / f_{FSR}$), φ_{ring} is the round-trip phase shift which indicates the resonance frequency offset of the ORR ($\varphi_{ring} = 2 \cdot \pi \cdot f_{res,offset} / f_{FSR}$), and k is the power coupling coefficient. The amplitude loss factor q is a function of the round-trip loss P_L :

$$q = 10^{-P_L/20}. \quad (2)$$

For a lossless ORR ($q = 1$) with a power coupling coefficient of 0.5, the calculated phase response of a single ORR ($\varphi_{ring} = 0$) over one FSR (red line), is shown in Figure 1b. As discussed before, the ORR is designed in such a way that one laser signal (f_{LD1}) is fixed at the ring's resonance frequency, while the other heterodyne signal (f_{LD2}) is fixed at the off-resonance frequency. By changing φ_{ring} through the ring heater, the phase response can be shifted, as shown in Figure 1b, by the purple and yellow lines. This allows it to impose different optical phase variations of the two laser signals, which are then transferred to the THz domain using the MUTC-PDs with $\Delta\varphi_{THz} = \Delta\varphi_{LD1} - \Delta\varphi_{LD2}$ [21]. Since the maximum phase tunable range of the laser signal 1 ($\Delta\varphi_{LD1,max}$) is 2π when changing φ_{ring} from $-\pi$ to

π which synchronously leads to variations of φ_{LD2} ($\Delta\varphi_{LD2} \neq 0$), it is necessary to use two cascaded ORRs for each OPS (blue line in Figure 1b) to achieve a THz phase shift $\Delta\varphi_{THz}$ of at least 2π . It can also be observed from Figure 1b that the FSR of the ORRs must be twice as large as the operating frequency, i.e., 0.6 THz, in order to fix one laser signal at resonance, and the one at off-resonance. The corresponding ORR round-trip length L for an FSR of 0.6 THz should be 0.282 mm in the optimum case, which can be calculated using

$$L = \frac{c_0}{n_g \cdot f_{FSR}}, \tag{3}$$

where n_g is the group index of TriPleX waveguides and equal to 1.777. However, the minimum round-trip length of a fabricated ORR must be larger than 7 mm, due to the required heater length for thermo-optical control. This leads to a maximum FSR of 24.1 GHz, which is much smaller than the optimum value. However, thanks to the periodicity of ORRs, the condition f_{LD2} at the off-resonance frequency and f_{LD1} at the resonance frequency can be satisfied, if an FSR meets the following condition:

$$|f_{LD1} - f_{LD2}| = (m + \frac{1}{2}) \cdot f_{FSR}, \tag{4}$$

where m is a natural number. As can be seen from Figure 1c, the phase shift of laser signal with f_{LD2} ($m = 13$) is equal to that with f_{LD2} ($m = 0$). Consequently, all ORRs in this work are designed with an FSR of 22.22 GHz.

To eventually use the fabricated OBFN chip for beam steering, the thermo-optically controlled power coupling coefficient k and the resonance frequency offset $f_{res,offset}$ must be determined for each ORR, as a function of the coupler and ring heater voltages, respectively. To determine the power coupling coefficient, the group delay τ_g is experimentally characterized using the wavelength-sweeping approach [22] for coupler heater voltages from 4 V to 12 V. The power coupling coefficient k can then be determined from the measured group delay using [20]

$$\tau_g(\Omega) = T + \frac{q \cdot \sqrt{1-k} \cdot \cos(\Omega + \varphi_{ring}) - (1-k)}{(1-k) - 2q \cdot \sqrt{1-k} \cdot \cos(\Omega + \varphi_{ring}) + q^2} \cdot T + \frac{q \cdot \sqrt{1-k} \cdot \cos(\Omega + \varphi_{ring}) - q^2 \cdot (1-k)}{1 - 2q \cdot \sqrt{1-k} \cdot \cos(\Omega + \varphi_{ring}) + q^2 \cdot (1-k)} \cdot T. \tag{5}$$

For the fabricated OBFN chip, the measured optical propagation loss is ~ 0.7 dB/cm. By considering the round-trip length of 7.59 mm, the round-trip loss P_L can be calculated to be 0.5 dB. This leads to an amplitude loss factor q of 0.944. The round-trip time T can be calculated using $T = 1/f_{FSR}$. Figure 2a shows the measured power coupling coefficient k as a function of the coupler heater bias. As can be seen, the power coupling coefficient increases from ~ 0.19 to ~ 1 by changing the bias voltage from 4 V to 12 V. Using a coupler heater bias of ~ 8.3 V, the power coupling coefficient can be set to 0.5.

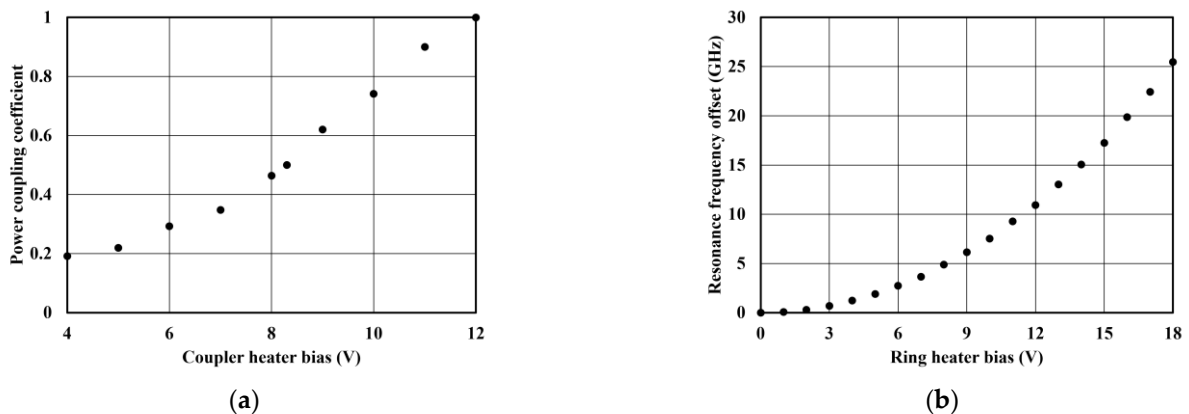


Figure 2. Measured power coupling coefficient as a function of coupler heater bias (a) and measured resonance frequency offset as a function of ring heater bias (b), of an ORR.

The resonance frequency offsets of ORRs are determined experimentally using a high-resolution optical spectrum analyzer (OSA, AP2060A, APEX Technologies, Marcoussis, France). Figure 2b shows the measured resonance frequency offset versus the ring heater bias. As can be seen, to shift the resonance frequency over one FSR, a bias voltage of ~17 V is required. For developing the control algorithm software, the measured resonance offset frequency is fitted using a sixth order polynomial equation

$$f_{\text{res.offset}} = 1 \cdot 10^{-6} \cdot U_r^6 - 7 \cdot 10^{-5} \cdot U_r^5 + 0.0013 \cdot U_r^4 - 0.0109 \cdot U_r^3 + 0.1147 \cdot U_r^2 - 0.0459 \cdot U_r + 0.0056, \quad (6)$$

where U_r is ring heater bias.

Based on the measurements, the power coupling coefficients of all ORRs are then set to 0.5 and the ring heaters are tuned to have the same resonance frequency in all ORRs. This is defined as the initial state for the OBFN chip, where the phase shifts of all OPSs are the same. Figure 3 shows the optical frequency response of one OPS at the initial state. As can be seen, the two resonance frequencies are at 193.4001 THz and 193.4220 THz, indicating an FSR of ~21.9 GHz. Due to this slight deviation from the designed value of 22.22 GHz (<1.5%), the fabricated OBFN chip is ideally suited for 295.65 GHz, according to Equation (4).

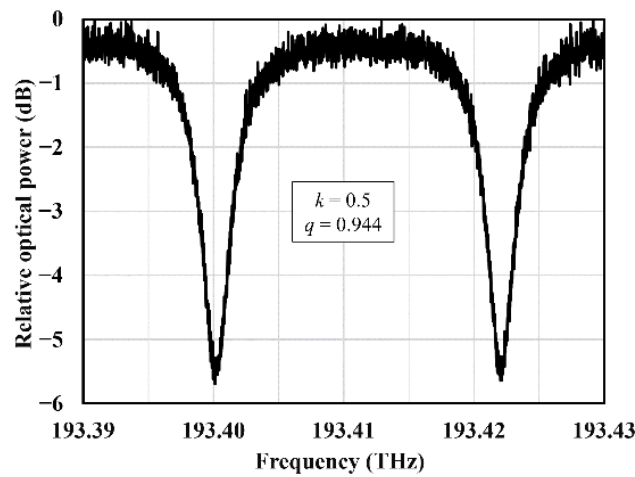


Figure 3. Measured optical frequency response of two cascaded ORRs at the same resonance frequency.

3. Phase Shift Characterization

To measure the phase shift between two PDs when changing the biases of ring heaters of the fabricated OBFN chip, the measurement setup shown in Figure 4 is used. Two optical heterodyne signals (@1.55 μm) are generated using two free running integrable tunable laser assemblies (PPCL200, Pure Photonics, San Jose, CA, USA). After amplification by an erbium-doped fiber amplifier (EDFA, EDFA100P, Thorlabs, Newton, NJ, USA), an optical polarization controller is used to ensure minimum optical losses due to the large polarization birefringence of TriPleX waveguides [23]. A heater control system is developed and implemented to precisely regulate the bias of each on-chip heater. The OBFN chip is mounted on a heat sink with a thermo-electric cooler (TEC) regulated by a temperature controller (TED4015, Thorlabs, Dachau/Munich, Germany) at ~20 °C. To measure the phase difference between the two waveguide ports (WPs), two PDs are fiber-chip coupled to WP1 and WP2. Optical delay lines (ODLs, Newport, Irvine, CA, USA) are used to compensate for the fiber length difference between the two PDs and the OBFN chip. A digital signal analyzer (DSA, DSA-Z 634A, Keysight, Santa Rosa, CA, USA) is used to measure the amplitudes of the PD-generated RF signals in time domain.

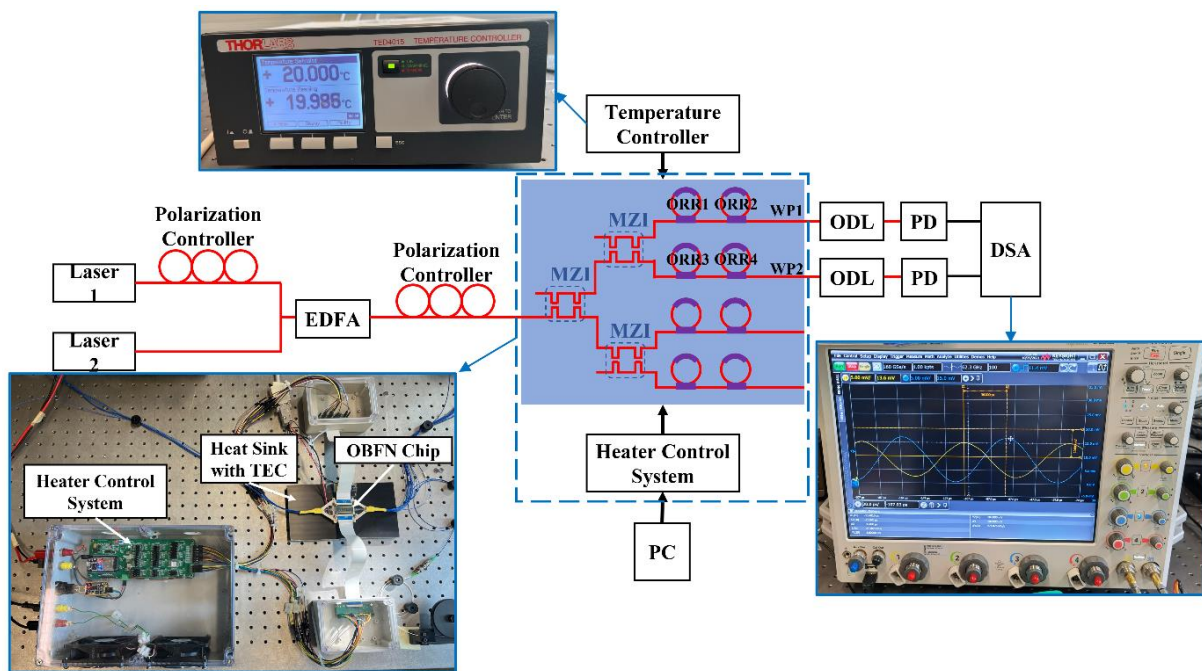


Figure 4. Measurement setup for phase shift characterization.

Before experimental characterization, all ORRs are set to be in the initial state with a power coupling coefficient of 0.5 and a resonance frequency of 193.4001 THz, using the heater control system. Since the analog bandwidth of the DSA is limited to 63 GHz, the phase shift between the two WPs cannot be measured directly in the THz domain. However, thanks to the periodicity of the ORRs, it is still possible to measure the THz phase shift using lower microwave frequencies. As explained above, all frequencies f_{LD1} and f_{LD2} that fulfill Equation (4) experience the same phase shift. This means when fixing f_{LD1} at 193.4001 THz (resonance frequency of the ORRs), the phase shift for $f_{LD2} = 193.41105$ THz (with $m = 0$) is same as for $f_{LD2} = 193.69575$ THz (with $m = 13$), as shown in Figure 1c. Therefore, the resulting phase shift for an RF signal at 10.95 GHz, is the same as for an RF frequency at 295.65 GHz.

During the measurements at an RF frequency of 10.95 GHz, the signal generated by the PD at WP1 (see Figure 4) is set as a trigger for the DSA, before tuning the two cascaded ORRs (ORR3 and ORR4) of the OPS for WP2. The RF signal measured this way is plotted in Figure 5a. As can be observed, the time delay of the 10.95 GHz signal is successfully changed when tuning the ORRs. The amplitude with a peak at the normalized time of 0 ps (black solid line) corresponds to the initial state of the OBFN chip. By increasing the ring heater biases, the time delay of the measured RF signal at 10.95 GHz is tuned to ~15.2 ps (blue solid line), ~30.5 ps (red solid line) and ~45.7 ps (green solid line). This corresponds to phase shifts of ~60°, ~120° and ~180°, respectively. Inverse phase shifts down to -180° can be achieved by reducing the ring heater biases, as shown by the dashed lines. Therefore, in total, a phase tuning of 2π is achieved. The corresponding ring heater bias settings are plotted in Figure 5b. As can be seen, the ring heater biases of the two ORRs are slightly different due to fabrication tolerances. To achieve a 2π phase shift, the ring heater bias of the ORR3 is changed from 3.42 V to 6.52 V, while the bias of the ORR4 is increased from 3.72 V to 6.79 V. Using the measured heater resistance of 540 Ω , the dissipative powers of the two heaters are calculated and plotted in Figure 5c. Consequently, a phase tuning efficiency of 0.058 W/ π is achieved.

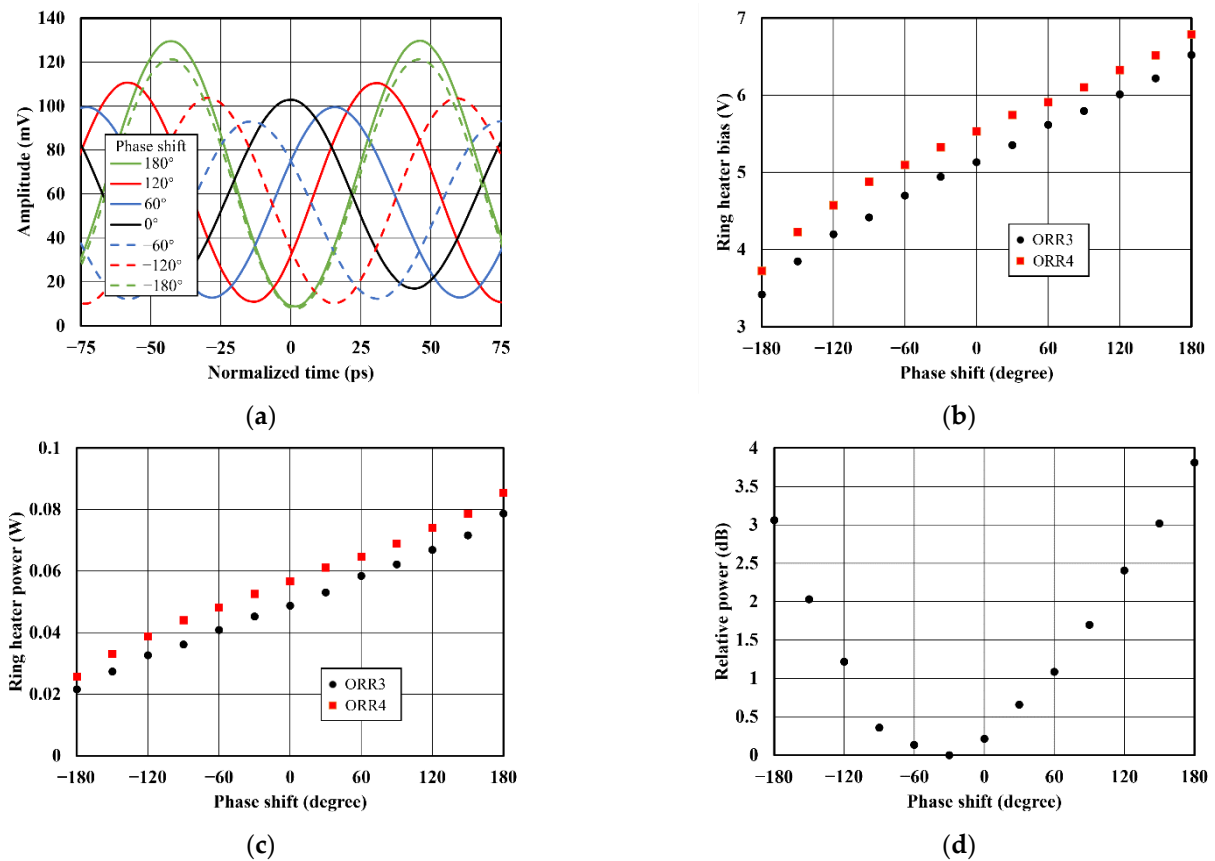


Figure 5. (a) Measured amplitudes of the 10.95 GHz signal (WP2) for various ring heater biases in time domain. (b) Measured ring heater biases of the ORR3 and ORR4 for phase shifts from -180° to 180° . (c) Calculated dissipative ring heater powers of the ORR3 and ORR4 for phase shifts from -180° to 180° . (d) Measured relative output power of a MUTC-PD at 0.295 THz for phase shifts from -180° to 180° .

From Figure 5a, it can be also observed that the amplitudes of the 10.95 GHz signal vary for different phase shifts. This is because the dispersive power transmission loss of the ORRs causes a power variation when tuning the phase, especially for the laser signal at resonance frequency. As can be seen, the maximum amplitude deviation is ~ 40.15 mV when comparing the amplitudes of the RF signals with phase shifts of 180° and -60° . To systematically analyze the impact of this inherent power variation on THz beam steering performance of a 1×4 phased array, we measured the output power of a MUTC-PD (J-band photomixer module, NTT Electronics, Yokohama, Japan) at 0.295 THz for different phase shifts, using a zero-biased Schottky-barrier diode (SBD, WR3.4 ZBD, Virginia Diodes, Charlottesville, VA, USA) as power detector. The results are plotted in Figure 5d. As can be seen, the minimum relative power is measured at a phase shift of -30° instead of 0° . This is traced back to the fact that the laser wavelength did not perfectly match the ORR’s resonance frequency during the experiments. For the full phase tuning range of 2π , the measured maximum THz output power variation is about 3.8 dB.

4. THz Beam Steering

Using CST Studio Suite, we numerically analyze the impact of the measured THz power variation on the beam steering performance. This is done for a 1×4 phased array featuring four bow-tie (BT) antennas with a pitch of $500 \mu\text{m}$ placed on a $100 \mu\text{m}$ thick InP substrate. To increase the directivity of this approach, InP-based dielectric rod waveguide (DRW) antennas are placed underneath the BT antennas (see inset in Figure 6). Each DRW antenna has a thickness d of $150 \mu\text{m}$ and a length l of $3500 \mu\text{m}$. The width w is $500 \mu\text{m}$. To

fix the DRW antennas in practice, they can be mounted using a low permittivity material such as ROHACELL [24], glued on the backside of the InP substrate.

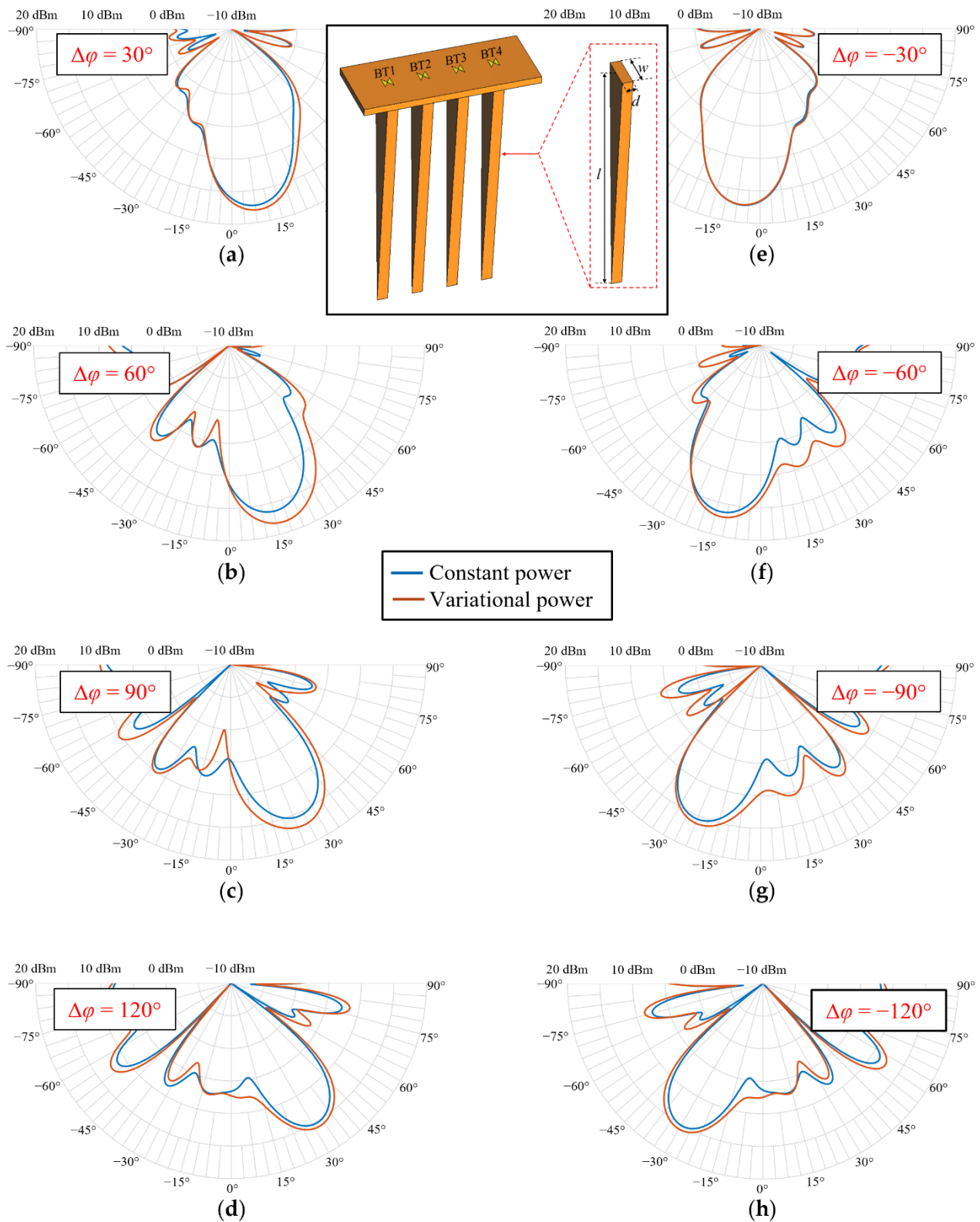


Figure 6. Simulated polar diagrams of absolute radiation powers of a 1×4 phased array with constant (blue lines) and variational (red lines) powers at 0.295 THz for phase differences between two adjacent antennas of (a) 30° , (b) 60° , (c) 90° , (d) 120° , (e) -30° , (f) -60° , (g) -90° and (h) -120° . The inset shows a schematic drawing of the 1×4 phased array with DRWs.

The beam steering behavior of the 1×4 array is investigated for two cases: (a) for a constant power at each BT antenna, and (b) when considering the measured power variations described in Section 3. In both scenarios, the phase difference between two adjacent antennas $\Delta\varphi$ is adjusted between -120° and 120° , with a step size of 30° . Phase differences larger than 120° would be possible using the fabricated OBFN, but would lead to substantially higher side lobes, and thus lower directivity and gain. Table 1 summarizes the parameters for each of the four antennas used in the simulations. For the constant power scenario, all antennas have the same constant input power of 0.21 dBm, independent from the phase difference. This value is defined by the power level at the phase shift of 0° when the power level at -30° is assumed to be 0 dBm (see Figure 5d). The phase of the BT1 maintains constant, and the phases of the other antennas are accordingly adjusted. For example, for a phase difference $\Delta\varphi$ of 30° , the phases of BT1 to BT4 are set to be $0^\circ, 30^\circ, 60^\circ$ and 90° . The corresponding polar diagrams of the absolute radiation power as a function of beam angle, which is the sum of the total input power of the four BT antennas in dBm and the simulated realized gain, are illustrated in Figure 6a–h for all phase differences (blue lines). As can be seen, the beam angle is 31° for a phase difference between two adjacent antennas of 120° . The maximum absolute radiation power is always in excess of 15.2 dBm, independent of the phase difference. When using negative phase shifts, the beam turns to the inverse direction. The maximum beam steering angle that can be achieved is $\sim 62^\circ$.

Table 1. Parameters for numerical analyses of constant power and variational power scenarios at 0.295 THz.

Phase Difference between Two Adjacent Antennas	Antenna												Figure
	BT1			BT2			BT3			BT4			
	Phase	Input Power (dBm)		Phase	Input Power (dBm)		Phase	Input Power (dBm)		Phase	Input Power (dBm)		
		Constant Power	Variational Power		Constant Power	Variational Power		Constant Power	Variational Power		Constant Power	Variational Power	
30°	0°	0.21	0.21	30°	0.21	0.66	60°	0.21	1.09	90°	0.21	1.70	Figure 6a
60°	0°	0.21	0.21	60°	0.21	1.09	120°	0.21	2.40	180°	0.21	3.81	Figure 6b
90°	0°	0.21	0.21	90°	0.21	1.70	180°	0.21	3.81	270°	0.21	0.36	Figure 6c
120°	0°	0.21	0.21	120°	0.21	2.40	240°	0.21	1.22	360°	0.21	0.21	Figure 6d
-30°	0°	0.21	0.21	-30°	0.21	0	-60°	0.21	0.13	-90°	0.21	0.36	Figure 6e
-60°	0°	0.21	0.21	-60°	0.21	0.13	-120°	0.21	1.22	-180°	0.21	3.06	Figure 6f
-90°	0°	0.21	0.21	-90°	0.21	0.36	-180°	0.21	3.06	-270°	0.21	1.70	Figure 6g
-120°	0°	0.21	0.21	-120°	0.21	1.22	-240°	0.21	2.40	-360°	0.21	0.21	Figure 6h

In the second scenario with varying antenna input powers, the simulated phase settings are the same as for the constant power scenario; only the input power for each antenna is set according to the measurement results, presented in Figure 5d, when the power level at -30° is assumed to be 0 dBm as well. It needs to be mentioned that due to the phase periodicity, the power levels at negative phases (from 0° to -180°) can be used for powers at phases between 180° and 360° , e.g., the measured value at -120° is used for the power level at 240° . The power levels for phases between -180° and -360° are determined in the same manner. The resulting polar diagrams of the absolute radiation power (red lines) are presented in Figure 6a–h as well. As can be seen, the radiation patterns, including the power variations, show a good agreement with those of where the power levels at each antenna are set to be constant. In general, the observed deviations of beam direction and maximum absolute radiation power are lower than 1° and 0.8 dB, respectively. Only for the phase differences of 60° and 90° , a larger power mismatch of <2 dB can be noticed, which is still reasonable. Thus, it is concluded that the inherent power variations when using the OBFN chip only have a minor impact on the steering performance of the phased array.

5. Discussion

In the last decade, thermo-optically controlled ORRs have been used to realize on-chip TTDs, supporting optical heterodyning for phased array at microwave frequencies to overcome the beam squint effect. For example, using two cascaded ORRs, the time delay is tunable up to 139.7 ps for a bandwidth of 8 GHz [15]. In [16], three ORRs are used in each delay unit for 41 GHz RF signals. A delay tuning range of 208.7 ps is demonstrated with a bandwidth of 6.3 GHz. In these two approaches, the time delay is managed by individually and diversely changing the power coupling coefficients of ORRs in each delay unit. Meanwhile, the resonance frequency of each ring must be adjusted synergistically and precisely to guarantee a reasonable ripple (within several picoseconds) for microwave frequencies. Another TTD for the 20 GHz band using a single ORR was demonstrated in [17]. A delay tuning range of 26.6 ps is achieved by changing the coupler bias voltage from 12 V to 16 V, with a bandwidth of 5 GHz. Since MZIs are used as tunable couplers, delay adjustment will lead to the drift of the ORR resonance frequency which must be compensated using the ring heater voltage. The aforementioned approaches, regardless of the number of ORRs used for TTDs, require two additional ORRs for the phase shift adjustment of the optical heterodyne carrier; this compensates for the nonlinearity of the phase response of TTDs [18], which further complicates the chip control, and increases the electrical power consumption.

In the THz domain, the beam angle becomes much more sensitive to time delay variations, as discussed in Section 1. At 0.3 THz, the signal period is 3.33 ps and the beam direction can be steered of $\sim 1^\circ$, with a time delay variation of only 30 fs. To achieve such high required delay tuning precisely, using ORR-based TTDs while keeping the ripple in the magnitude of femtoseconds, substantially more complex control circuitry is essential.

Due to the less dominant beam squint effect in the THz domain [9], we developed the OPSs with two cascaded and identical ORRs in each, offering comparably simple control circuitry. Here, the coupler heater voltages are maintained constant after setting the power coupling coefficient of 0.5. A phase tuning range up to 2π is achieved by uniformly adjusting the resonance frequencies of two ORRs, without the complicated and synergistic handling needed for TTDs. Compared with the OPSs based on straight waveguides, with only one heater for each control unit [10], the approach presented in this work demonstrates two inimitable merits. Firstly, the sharper phase response slope around resonance frequencies of ORRs, compared to that of straight waveguides, enables a higher phase tuning efficiency. In addition, the ORR-based OPSs are able to impose different optical phase variations on two combined optical heterodyne signals, due to the dispersive phase response of ORRs. Therefore, only one optical input is required for the OBFN chip, leading to a concise layout, as shown in Figure 1a. In contrast to that, the OPSs based on straight waveguides can be used only for the phase tuning of one optical carrier. Other passive optical waveguides are necessary to combine the second optical heterodyne signal behind each OPS. Consequently, two optical inputs are necessary for the OBFN chip. This leads to inevitable waveguide intersections on the chip and higher optical loss, especially for large phased arrays.

The OBFN chip reported in this work can be further optimized by replacing the MZIs used in each ORR as tunable couplers by 3 dB directional couplers, since the power coupling coefficients of all ORRs maintain 0.5 during the phase tuning. This way, the footprint and the power consumption of the chip can be further reduced. In Table 2, a summary of the OBFN chips discussed above is given.

Table 2. Comparison of OBFN chips supporting optical heterodyning for phased arrays.

Ref.	Frequency (GHz)	Control Unit	Number of Heaters in Each Control Unit	Waveguide Intersection	Tuning Efficiency	Control Circuitry
[15]	N/A (Microwaves)	TTD	8 (4 for TTD, 4 for SCT)	No	Low	Complicated
[16]	41	TTD	10 (6 for TTD, 4 for SCT)	No	Low	Complicated
[17]	20	TTD	6 (2 for TTD, 4 for SCT)	No	Low	Complicated
[10]	300	OPS	1	Yes	Intermediate (0.24 W/ π)	Simple
This work	300	OPS	4/2 *	No	High (0.058 W/ π)	Comparably simple

* The heater number can be reduced to two using 3 dB directional couplers instead of MZIs for ORRs.

6. Conclusions

In this manuscript, we reported on the design and experimental characterization of a 1×4 OBFN chip for continuous beam steering at 0.3 THz. The TriPleX-based OBFN chip consists of four OPSs and three MZIs, to control the phase and the power of the optical heterodyne THz signal at each transmit antenna, respectively. Two cascaded ORRs are used for each OPS to reach a maximum THz phase shift of at least 2π . The ORRs are designed in a way to only impose a tunable phase shift on one of the optical heterodyne signals, whereas the phase of the second optical carrier remains quasi-unchanged. Experimentally, THz phase tuning up to 2π with a tuning efficiency of only $0.058 \text{ W}/\pi$ per OPS, is demonstrated. A maximum inherent power variation of 3.8 dB is experimentally observed at 0.295 THz, when changing the phase. This is traced back to the dispersive power transmission loss of the ORRs. It is shown numerically using CST Studio Suite that the power variations only have a minor impact on the steering performance. The deviations in beam direction and maximum absolute radiation power of a 1×4 phased array are found to be below 1° and 2 dB, respectively. The manuscript also reports on the simulated far-field radiation patterns using the OBFN chip connected to the 1×4 phased array. Each BT antenna is connected to a DRW to increase the directivity. The observed total beam steering angle at 0.295 THz is $\sim 62^\circ$, when changing the phase difference between two adjacent antennas from -120° to 120° .

Author Contributions: Conceptualization, P.L. and A.S.; methodology, P.L. and C.R.; software, T.H.; formal analysis, P.L.; investigation, P.L.; resources, P.L., T.H. and J.T.; data curation, P.L. and T.H.; writing—original draft preparation, P.L.; writing—review and editing, P.L., T.H., J.T., C.R. and A.S.; visualization, P.L. and T.H.; supervision, A.S.; project administration, A.S.; funding acquisition, A.S. All authors have read and agreed to the published version of the manuscript.

Funding: This research was funded by the Federal Ministry of Education and Research within the projects “Open6GHub” (grant No.16KISK017) and “6GEM” (grant No.16KISK039 439), and by the Deutsche Forschungsgemeinschaft (DFG, German Research Foundation) under Project-ID 287022738–CRC/TRR 196 (Project C07).

Institutional Review Board Statement: Not applicable.

Informed Consent Statement: Not applicable.

Data Availability Statement: Not applicable.

Acknowledgments: The authors would like to thank Marcel Hoekman from LioniX International BV, The Netherlands, for the support in chip design and support by the Open Access Publication Fund of the University of Duisburg-Essen.

Conflicts of Interest: The authors declare no conflict of interest.

References

1. Ducournau, G.; Szriftgiser, P.; Beck, A.; Bacquet, D.; Pavanello, F.; Peytavit, E.; Zaknour, M.; Akalin, T.; Lampin, J.-F. Ultrawide-bandwidth single-channel 0.4-THz wireless link combining broadband quasi-optic photomixer and coherent detection. *IEEE Trans. Terahertz Sci. Technol.* **2014**, *4*, 328–337. [CrossRef]
2. Harter, T.; Füllner, C.; Kemal, J.; Ummethala, S.; Steinmann, J.; Brosi, M.; Hesler, J.; Bründermann, E.; Müller, A.-S.; Freude, W. Generalized Kramers–Kronig receiver for coherent terahertz communications. *Nat. Photonics* **2020**, *14*, 601–606. [CrossRef]
3. Hermans, R.I.; Seddon, J.; Shams, H.; Ponnampalam, L.; Seeds, A.J.; Aeppli, G. Ultra-high-resolution software-defined photonic terahertz spectroscopy. *Optica* **2020**, *7*, 1445–1455. [CrossRef]
4. Song, H.-J.; Shimizu, N.; Furuta, T.; Suizu, K.; Ito, H.; Nagatsuma, T. Broadband-frequency-tunable sub-terahertz wave generation using an optical comb, AWGs, optical switches, and a uni-traveling carrier photodiode for spectroscopic applications. *J. Light. Technol.* **2008**, *26*, 2521–2530. [CrossRef]
5. Dülme, S.; Steeg, M.; Mohammad, I.; Schriniski, N.; Tebart, J.; Stöhr, A. Ultra-low phase-noise photonic terahertz imaging system based on two-tone square-law detection. *Opt. Express* **2020**, *28*, 29631–29643. [CrossRef] [PubMed]
6. Lu, P.; Haddad, T.; Tebart, J.; Steeg, M.; Sievert, B.; Lackmann, J.; Rennings, A.; Stöhr, A. Mobile THz communications using photonic assisted beam steering leaky-wave antennas. *Opt. Express* **2021**, *29*, 21629–21638. [CrossRef] [PubMed]
7. Zhou, Y.; Sakano, G.; Yamanaka, Y.; Ito, H.; Ishibashi, T.; Kato, K. 600-GHz-Wave Beam Steering by Terahertz-Wave Combiner. In Proceedings of the OFC, San Diego, CA, USA, 11–15 March 2018; pp. 1–3.
8. Liu, Y.; Isaac, B.; Kalkavage, J.; Adles, E.; Clark, T.; Klamkin, J. True Time Delay Millimeter Wave Beam Steering with Integrated Optical Beamforming Network. In Proceedings of the CLEO: Science and Innovations, San Jose, CA, USA, 5–10 May 2019; p. SF3N.6.
9. Lu, P.; Haddad, T.; Tebart, J.; Stöhr, A. Photonic Integrated Chips for THz Beam Steering. In Proceedings of the Asia Communications and Photonics Conference, Shanghai China, 24–27 October 2021; p. M5E.3.
10. Che, M.; Matsuo, Y.; Kanaya, H.; Ito, H.; Ishibashi, T.; Kato, K. Optoelectronic THz-wave beam steering by arrayed photomixers with integrated antennas. *IEEE Photonics Technol. Lett.* **2020**, *32*, 979–982. [CrossRef]
11. Zhuang, L. Flexible RF filter using a nonuniform SCISSOR. *Opt. Lett.* **2016**, *41*, 1118–1121. [CrossRef] [PubMed]
12. Zhuang, L.; Zhu, C.; Corcoran, B.; Burla, M.; Roeloffzen, C.G.; Leinse, A.; Schröder, J.; Lowery, A.J. Sub-GHz-resolution C-band Nyquist-filtering interleaver on a high-index-contrast photonic integrated circuit. *Opt. Express* **2016**, *24*, 5715–5727. [CrossRef] [PubMed]
13. Taddei, C.; Zhuang, L.; Hoekman, M.; Leinse, A.; Oldenbeuving, R.; van Dijk, P.; Roeloffzen, C. Fully reconfigurable coupled ring resonator-based bandpass filter for microwave signal processing. In Proceedings of the Microwave Photonics (MWP) and the 2014 9th Asia-Pacific Microwave Photonics Conference (APMP) 2014 International Topical Meeting, Hokkaido, Japan, 20–23 October 2014; pp. 44–47.
14. Zhuang, L.; Roeloffzen, C.G.; Hoekman, M.; Boller, K.-J.; Lowery, A.J. Programmable photonic signal processor chip for radiofrequency applications. *Optica* **2015**, *2*, 854–859. [CrossRef]
15. Burla, M.; Marpaung, D.A.; Zhuang, L.; Khan, M.R.; Leinse, A.; Beeker, W.; Hoekman, M.; Heideman, R.G.; Roeloffzen, C.G. Multiwavelength-integrated optical beamformer based on wavelength division multiplexing for 2-D phased array antennas. *J. Light. Technol.* **2014**, *32*, 3509–3520. [CrossRef]
16. Liu, Y.; Wichman, A.R.; Isaac, B.; Kalkavage, J.; Adles, E.J.; Clark, T.R.; Klamkin, J. Ultra-low-loss silicon nitride optical beamforming network for wideband wireless applications. *IEEE J. Sel. Top. Quantum Electron.* **2018**, *24*, 8300410. [CrossRef]
17. Tessema, N.; Cao, Z.; Van Zantvoort, J.; Mekonnen, K.; Dubok, A.; Tangdionga, E.; Smolders, A.; Koonen, A. A tunable Si₃N₄ integrated true time delay circuit for optically-controlled K-band radio beamformer in satellite communication. *J. Lightwave Technol.* **2016**, *34*, 4736–4743. [CrossRef]
18. Burla, M.; Marpaung, D.; Zhuang, L.; Roeloffzen, C.; Khan, M.R.; Leinse, A.; Hoekman, M.; Heideman, R. On-chip CMOS compatible reconfigurable optical delay line with separate carrier tuning for microwave photonic signal processing. *Opt. Express* **2011**, *19*, 21475–21484. [CrossRef] [PubMed]
19. Roeloffzen, C.G.; Hoekman, M.; Klein, E.J.; Wevers, L.S.; Timens, R.B.; Marchenko, D.; Geskus, D.; Dekker, R.; Alippi, A.; Grootjans, R. Low-loss Si₃N₄ TriPleX optical waveguides: Technology and applications overview. *IEEE J. Sel. Top. Quantum Electron.* **2018**, *24*, 4400321. [CrossRef]
20. Han, X.; Zhang, J.; Song, H.; Wang, L.; Teng, J.; Wu, P.; Zhao, M. Influence of coupling conditions on the time delay characteristics of parallel-cascaded optical waveguide ring resonators. *Optik* **2013**, *124*, 377–384. [CrossRef]
21. Kolpatzek, K.; Haring, L.; Czylwik, A. Phase control in photonically steered phased array transmitters by optical homodyne detection. In Proceedings of the 2016 46th European Microwave Conference (EuMC), London, UK, 4–6 October 2016; pp. 1095–1098.
22. Zhuang, L.; Roeloffzen, C.G.; Meijerink, A.; Burla, M.; Marpaung, D.A.; Leinse, A.; Hoekman, M.; Heideman, R.G.; van Etten, W. Novel ring resonator-based integrated photonic beamformer for broadband phased array receive antennas—Part II: Experimental prototype. *J. Lightwave Technol.* **2009**, *28*, 19–31. [CrossRef]
23. Wörhoff, K.; Heideman, R.G.; Leinse, A.; Hoekman, M. TriPleX: A versatile dielectric photonic platform. *Adv. Opt. Technol.* **2015**, *4*, 189–207. [CrossRef]
24. Pronat Industries. Available online: <https://pronatindustries.com/wp-content/uploads/2014/12/ROHACELL-HF-Product-Information-datasheet.pdf> (accessed on 4 October 2022).

DuEPublico

Duisburg-Essen Publications online

UNIVERSITÄT
DUISBURG
ESSEN

Offen im Denken

ub | universitäts
bibliothek

This text is made available via DuEPublico, the institutional repository of the University of Duisburg-Essen. This version may eventually differ from another version distributed by a commercial publisher.

DOI: 10.3390/photonics9120902

URN: urn:nbn:de:hbz:465-20230622-162329-9



This work may be used under a Creative Commons Attribution 4.0 License (CC BY 4.0).